



## Radio Science

### RESEARCH ARTICLE

10.1002/2017RS006488

#### Special Section:

URSI General Assembly and  
Scientific Symposium (2017)

#### Key Points:

- Characterization of short-wave fadeout (SWF) is seen in the suppression of SuperDARN daytime ground scatter
- Features of SWF seen in SuperDARN observations vary with solar zenith angle, radar operating frequency, and peak solar flare intensity
- A pronounced Doppler flash is observed in the velocity measurement and precedes the main phase of the SWF effect in the ground scatter

#### Correspondence to:

S. Chakraborty,  
shibaji7@vt.edu

#### Citation:

Chakraborty, S., Ruohoniemi, J. M., Baker, J. B. H., & Nishitani, N. (2018). Characterization of short-wave fadeout seen in daytime SuperDARN ground scatter observations. *Radio Science*, 53, 472–484. <https://doi.org/10.1002/2017RS006488>

Received 27 OCT 2017

Accepted 17 MAR 2018

Accepted article online 23 MAR 2018

Published online 18 APR 2018

## Characterization of Short-Wave Fadeout Seen in Daytime SuperDARN Ground Scatter Observations

S. Chakraborty<sup>1</sup>, J. M. Ruohoniemi<sup>1</sup>, J. B. H. Baker<sup>1</sup>, and N. Nishitani<sup>2</sup>

<sup>1</sup>Bradley Department of Electrical and Computer Engineering, Virginia Polytechnic Institute and State University, Blacksburg, VA, USA, <sup>2</sup>Solar Terrestrial Environment Laboratory, Nagoya University, Nagoya, Japan

**Abstract** Short-wave fadeout (SWF) is a well-known radio wave anomaly which follows Earth-directed solar flares and leads to severe disruption of transionospheric high-frequency systems. The disruption is produced by flare-enhanced soft and hard X-rays that penetrate to the *D* layer where they dramatically enhance ionization leading to heavy high-frequency absorption over much of the dayside for an hour or more. In this paper, we describe how Super Dual Auroral Radar Network (SuperDARN) observations can be exploited to analyze SWF events. Superposed epoch analysis of multiple signatures reveals the typical characteristics of SWF. The number of SuperDARN ground scatter echoes drops suddenly ( $\approx 100$  s) and sharply after a solar flare, reaching a maximum depth of suppression within a few tens of minutes, and then recovering to pre-SWF conditions over half an hour or so. The depth of echo suppression depends on the solar zenith angle, radio wave frequency, and intensity of the flare. Furthermore, ground scatter echoes typically exhibit a sudden phase change leading to a dramatic increase in apparent Doppler velocity (the so-called “Doppler flash”), which statistically precedes the dropout in ground scatter echoes. We report here on the characterization of SWF effects in SuperDARN ground scatter observations produced by several X class solar flares. We also describe the functional dependence of peak Doppler flash on solar zenith angle, frequency, and peak intensity of solar flux.

**Plain Language Summary** This study is about how energetic electromagnetic eruptions (solar flares) coming from the Sun alter the physical properties of the ionosphere which affects the over the horizon high-frequency (HF) radio communication channels, commonly known as short-wave fadeout (SWF). The study characterizes different facts and features of SWF seen in daytime observations of the SuperDARN HF radar (a monostatic HF transceiver system, which simulates a two-way HF communication link) during different solar flare events. The article also demonstrates how the physical location of HF transmitter/receiver, HF transmitter frequency, and intensity of solar flare impacts SWF.

### 1. Introduction

A solar flare event is a sudden increase in brightness observed near the Sun's surface across a broad spectrum of frequencies (Mittra, 1974; Newton & Barton, 1937), lasting for a few minutes to several hours. Enhanced fluxes of solar X-rays penetrate deep into the Earth's atmosphere (reaching down to the *D* region) where they dramatically increase ionization on the dayside. This sudden increase of plasma density causes an increase in radio wave absorption (Benson, 1964; McNamara, 1978), which is most severe in the 3–30 MHz high-frequency (HF) ranges, commonly known as short-wave fadeout (SWF). The enhancement of *D* region plasma also increases the bending of radio waves due to changes in refractive index of the ionosphere. Solar extreme ultraviolet (EUV) and X-rays propagate at the speed of light and take only  $\approx 8$  min to reach Earth's atmosphere, so SWF is one of the earliest space weather effects following a flare. This geophysical phenomenon was first described by J. H. Dellinger in 1935 (Dellinger, 1937) and a later statistical study (DeMastus & Wood, 1960) showed that there is a one-to-one relation between solar flares and SWF. A recent study by Zawdie et al. (2017) showed that plasma density enhancement is the main driver of HF radio wave absorption in *D* and *E* layers. Developing an improved understanding of SWF is important because these events have serious effects on transionospheric radio wave systems including ground-to-ground radio communications (Davies, 1990; Ellison, 1996), amateur radio links, satellite communication systems, and Global Navigation Satellite Systems (GNSS; Tsurutani et al., 2006).

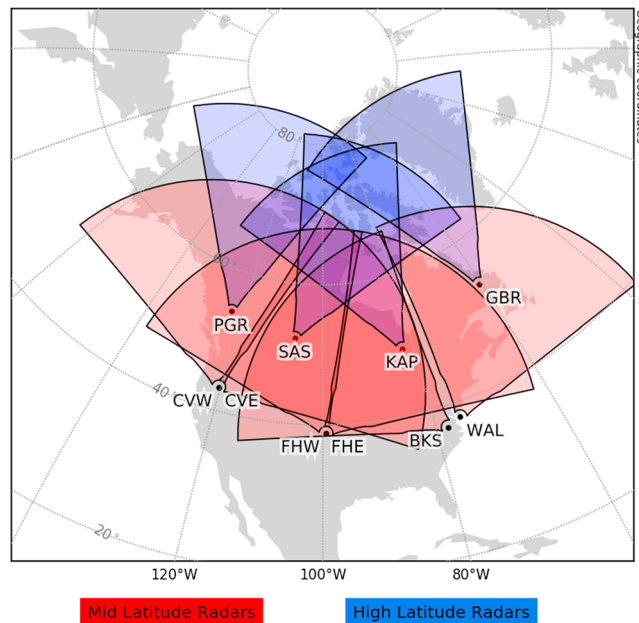


**Figure 1.** Fields-of-view (FoV) of SuperDARN radars located at middle (red) and high (blue) latitudes used in this study. The radars are Prince George (PGR), Saskatoon (SAS), Kapuskasing (KAP), Goose Bay (GBR), Christmas Valley East and West (CVE, CVW), Fort Hays East and West (FHE, FHW), Blackstone (BKS), and Wallops Island (WAL).

Many instruments have been used to study SWF. In the early 1950s the riometer (Mitra & Shain, 1953) was the main instrument to study the cause of ionospheric absorption, but recently incoherent scatter radar data (Mendillo & John, 1974) have been used to study the increase in *D* region ionization more directly. Digisonde (digital ionosonde) and GNSS total electron content (TEC) data (Afraimovich, 2000) have also been used to study fluctuations of the ionospheric plasma frequency profile during flare events. Handzo et al. (2014) used a digisonde and incoherent scatter radar-based system to characterize the enhancement of plasma frequency and *D* region absorption, whereas Xiong et al. (2013) used ionospheric solar flare activity indicator (ISFAI, GNSS TEC data) to characterize flare-related anomalies in TEC data. Modeling has been used in an effort to better understand the physics of ionospheric absorption and its variability during SWF events (Siskind et al., 2017). Eccles et al. (2005) used ionospheric radio sounding data to study the characteristics of SWF and as input to a data-driven photochemical model of *D* region absorption. Finally, Watanabe and Nishitani (2013) used Super Dual Auroral Radar Network (SuperDARN) radar data to study SWF and establish the fact that Doppler characteristics of SWF observed on HF radar are highly correlated with *D* region plasma enhancement. Despite these efforts the physics behind SWF is not yet fully understood, and tools for widespread monitoring of SWF effects on HF propagation are lacking.

In this paper, we present a comprehensive statistical characterization of SWF using the SuperDARN HF over the horizon radar system. Specifically, we characterize SWF events in terms of solar zenith angle, transmitted frequency, and flare intensity and examine the timings of SWF across the dense subnetwork of SuperDARN radars in North America. We discuss one illustrative event study in detail and present some statistical characteristics of SWF events seen in SuperDARN radar observations.

## 2. Instrumentation: SuperDARN

The SuperDARN is a network of high-frequency (HF, 8–20 MHz) radar designed to probe the Earth's ionosphere and its relationship to space (Chisham et al., 2007; Greenwald et al., 1985). SuperDARN radars measure the line-of-sight velocity component of the *F* region drift of ionospheric plasma when decameter-scale electron density irregularities are present and oriented favorably to produce backscatter. Although the network was originally constructed to image the high-latitude auroral zone, it has recently been expanded to middle latitudes. Figure 1 shows the dense subnetwork of middle- and high-latitude SuperDARN radars in the North American sector used for this study. Also, the large spatial extent and continuous operation of the SuperDARN radar chain makes it a well-suited network for detecting and monitoring the flare effects in real time.

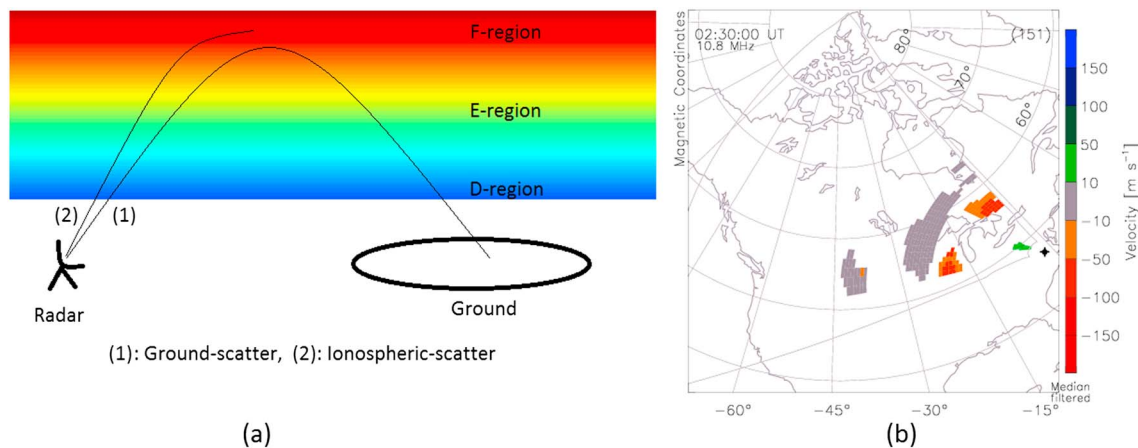


**Figure 2.** (a) Schematic plot of SuperDARN radar show ray paths of ground scatter and ionospheric scatter, (b) SuperDARN field-of-view scan plot, showing line-of-sight Doppler velocity measured by the Blackstone radar on 31 May 2017 at 2:30 UT. Velocity is color coded according to the scale on the right and ground scatter is marked gray.

SuperDARN radars observations primarily consist of two types of backscatter signals, namely, ground scatter and ionospheric scatter as shown in Figures 2a and 2b. Figure 2a shows how ground scatter and ionospheric scatter are generated in the HF radar observations. In the case of ground scatter [corresponds to ray (1) of Figure 2a], due to vertical gradient in refractive index, the ray bends toward the ground and is reflected from the surface roughness and returns back to the radar following the same path. This simulates a complete one-hop ground-to-ground HF communication link, which passes through the D region 4 times. Ionospheric scatter [corresponds to ray (2) of Figure 2a] is due to the reflection of signal from ionospheric plasma irregularities and are associated with relatively higher Doppler velocities and wider spectral width. Figure 2b presents a SuperDARN field-of-view Doppler velocity scan plot from the Blackstone radar showing ground scatter (in gray) and ionospheric scatter (in color) color coded by Doppler velocity. During daytime SuperDARN observations typically feature a band of ground scatter that extends over several hundred kilometer range. The effects of SWF can be easily identified in this ground scatter band. To select the ground scatter we identified SuperDARN observations having relatively low Doppler velocity (within  $\pm 10$  m/s range) and, narrow spectral width. Typical daytime ground scatter band lies within the slant range  $>900$  km and  $<2,000$  km from slightly after the sunrise to sunset.

### 3. Results

This section is split into two subsections: (1) A case study of an SWF event which occurred in response to an X class solar flare (X2.7) on 5 May 2015 at 22:10 UT and (2) a statistical study of multiple SWF signatures observed by SuperDARN radars across North America.

#### 3.1. Event Study: An Example of Short-Wave Fadeout on 5 May 2015

In this part we present an event study of an X class solar flare signature in SuperDARN data. Figure 3 presents a typical example of an SWF event seen by the Blackstone radar in response to a solar flare measured by GOES spacecraft at 22:10 UT on 5 May 2015. The upper nine panels (Figure 3a) present a series of field-of-view scan plots of line-of-sight Doppler velocity at 4-min cadence, while the lower two panels (Figure 3b) show range time plots of received power and Doppler velocity on beam 7. Figure 3a shows a complete wipeout of backscatter signal at 22:12 UT, consistent with SWF, while Figure 3b shows that the SWF phenomenon lasts on the order of tens of minutes and gradually restores back to normal (pre-SWF) condition with some negative shifts in Doppler velocity. Also noteworthy is the fact that the radio blackout event was preceded by a sudden enhancement of apparent backscatter Doppler velocity at 22:08 UT, which is evident in both Figures 3a and 3b. Because this “Doppler Flash” signature is embedded within a robust band of preexisting ground scatters, it must be associated with a sudden change in the environmental condition along the ray path due to change in phase path length (due to ionospheric properties, such as refractive index) and not due to a displacement of the ray path itself.

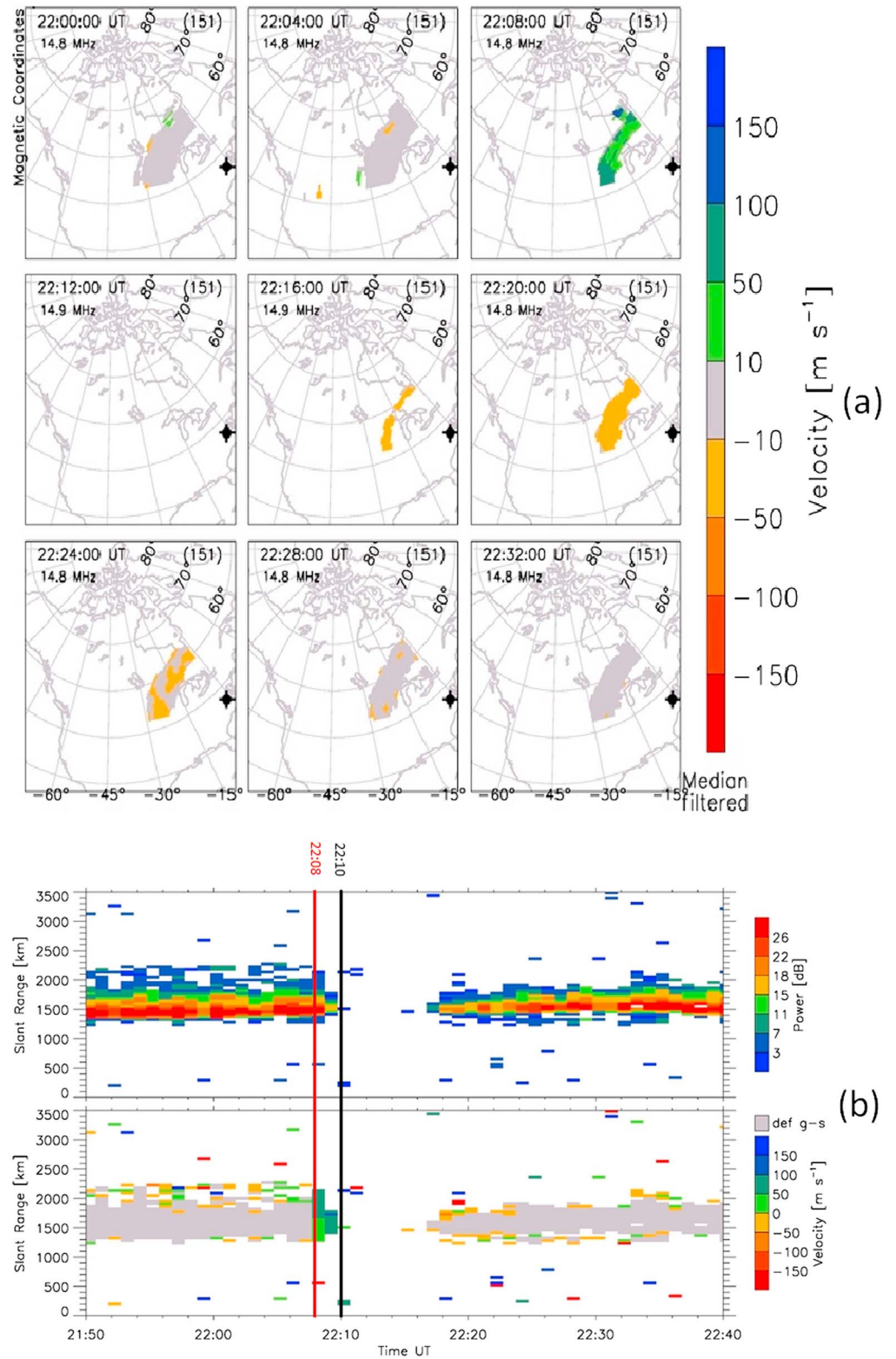


**Figure 3.** Response of the Blackstone radar to a solar flare on 5 May 2015: (a) Series of field-of-view scan plots of line-of-sight Doppler velocity color coded according to the scale on the right and (b) Range-Time (RTI) plot showing backscattered power (top panel) and Doppler velocity (bottom panel) on beam 7, color coded according to the scales on the right. The vertical line denotes the start of the Doppler flash in red and start of the radio blackout phase in black, respectively.



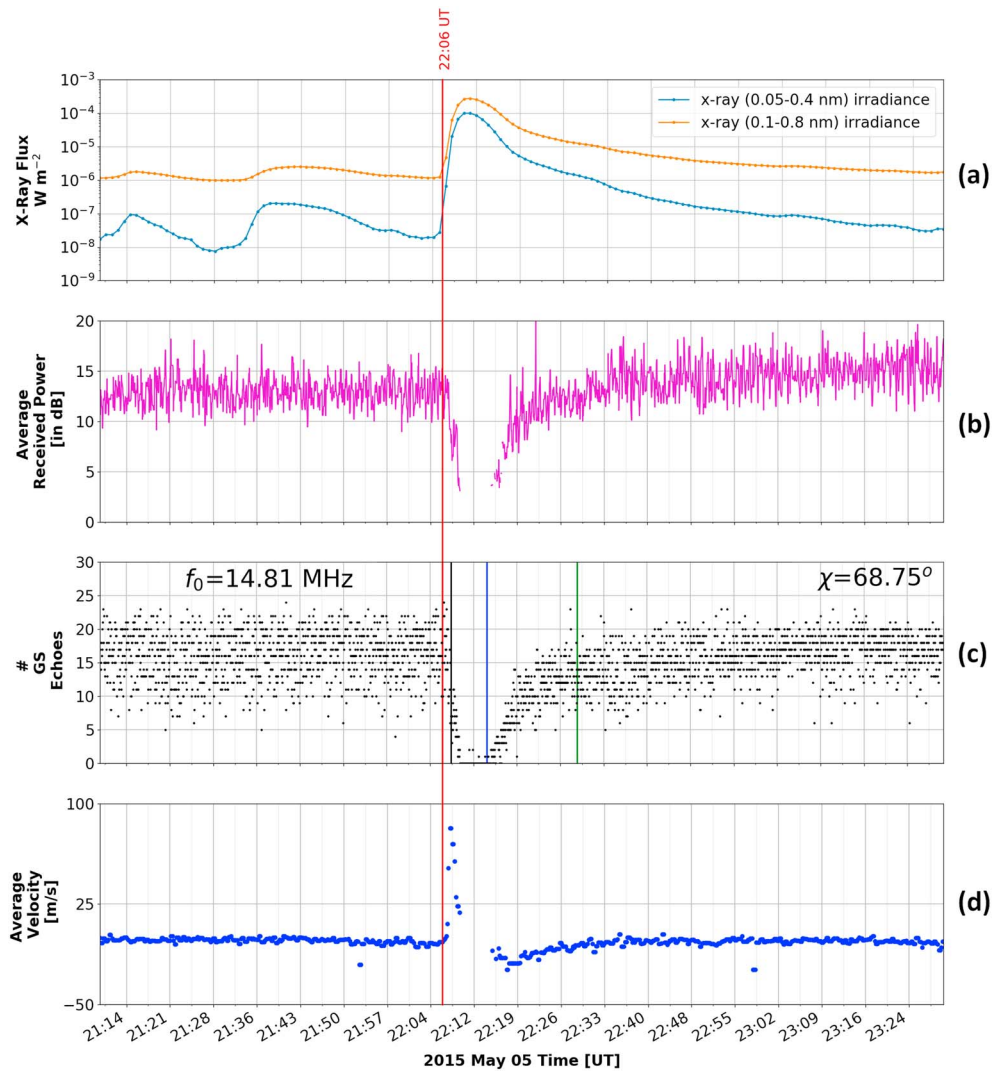


**Figure 4.** GOES and Blackstone (BKS) radar measurements during a solar flare and associated SWF event on 5 May 2015: (a) GOES X-ray flux 0.1–0.8 nm (orange) and 0.05–0.4 nm (blue) wavelength bands, (b) average backscatter BKS power, (c) average number of BKS ground scatter echoes, and (d) average BKS line-of-sight Doppler velocity. Vertical lines in panel (c) represent onset time (red), blackout start time (black), blackout end time (blue), and recovery time (green). The radar operating frequency ( $f_0$ ) and solar zenith angle ( $\chi$ ) are provided. The red line passing through all the panels represents the event commencement timing (22:08 UT). See section 3.1 for details.

Figure 4 compares the Blackstone (BKS) measurements to GOES X-ray fluxes. The event can be seen to initiate at 22:06 UT when the GOES X-ray sensor observes a sudden increase in solar X-ray flux (panel a), and BKS starts to observe a decrease in average received power (panel b) and number of ground scatter echoes (panel c) leading to a total wipeout of radio link about 10 min and a gradual recovery over 30–60 min. Finally, panel (d) shows the “Doppler Flash” signature peaks at a value of 80–100 m/s on a similar time scale as the SWF. We discuss the physics behind this Doppler phenomenon in section 4. The vertical red line passing through all panels represents SWF “onset time” when a significant depletion in the number of ground scatter echoes is first detected. Other vertical lines in panel (c) represent “radio blackout start time” (black), “onset of recovery time” (blue), and “recovery time” (green) of the SWF phenomenon. The radio blackout start time corresponds to nearly complete suppression ( $\geq 80\%$  reduction) in the number of ground scatter echoes; the onset of recovery time corresponds to the beginning of the recovery phase ( $\geq 25$ – $30\%$  increase); and the recovery time corresponds to the time when ground scatter reaches almost back to preexisting conditions ( $\geq 95\%$  of pre-SWF count). More importantly, the event onset timing matches the time of solar flare onset. In this particular case, the duration of the onset, blackout, and recovery phase are 1.4, 13.9, and 26.3 min, respectively.

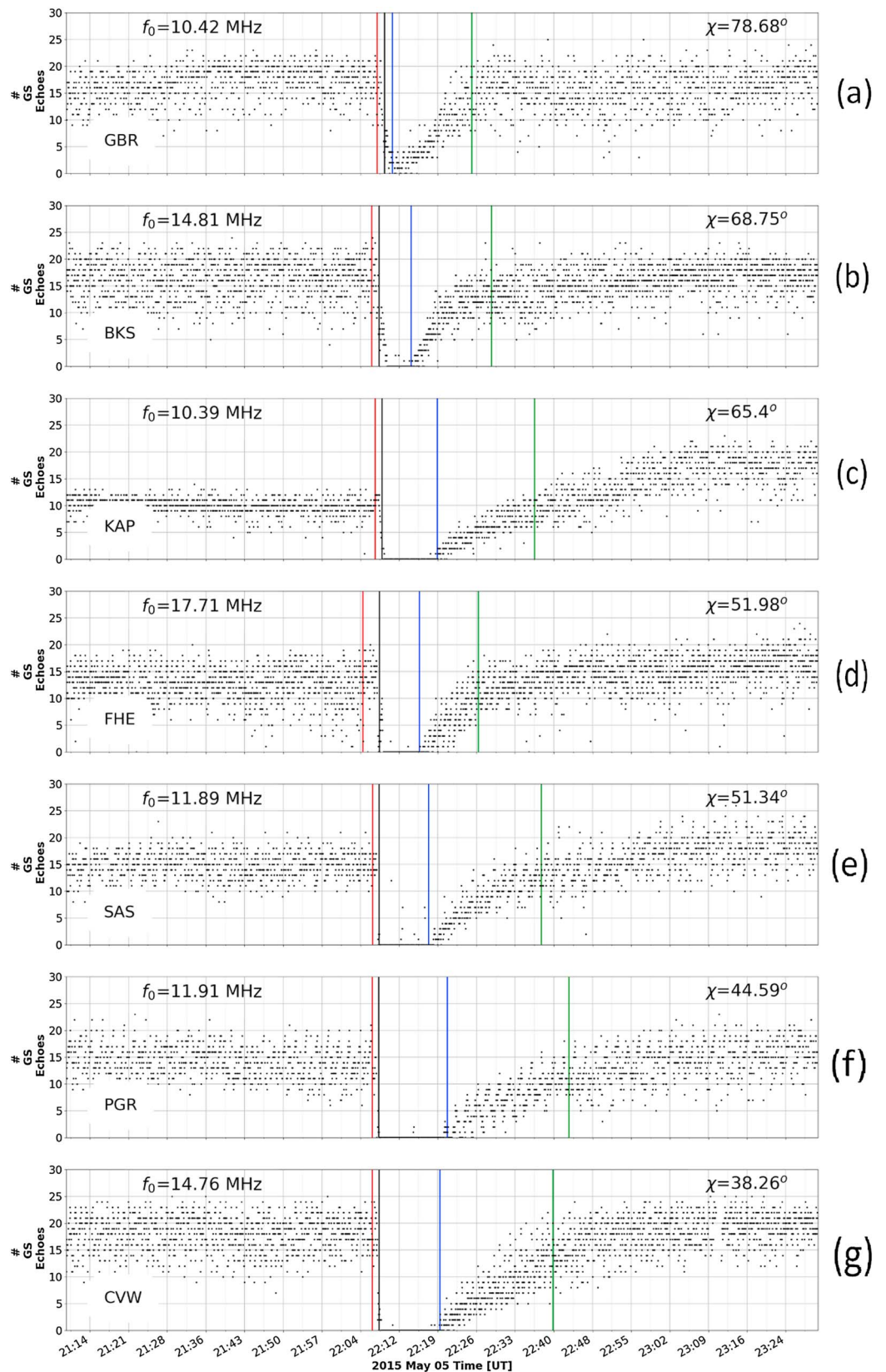


**Figure 5.** Multiradar time series of the ground scatter echoes during a SWF event on 5 May 2015 observed by the (a) GBR, (b) BKS, (c) KAP, (d) FHE, (e) SAS, (f) PGR, and (g) CVW radars. Similar format to Figure 4c.

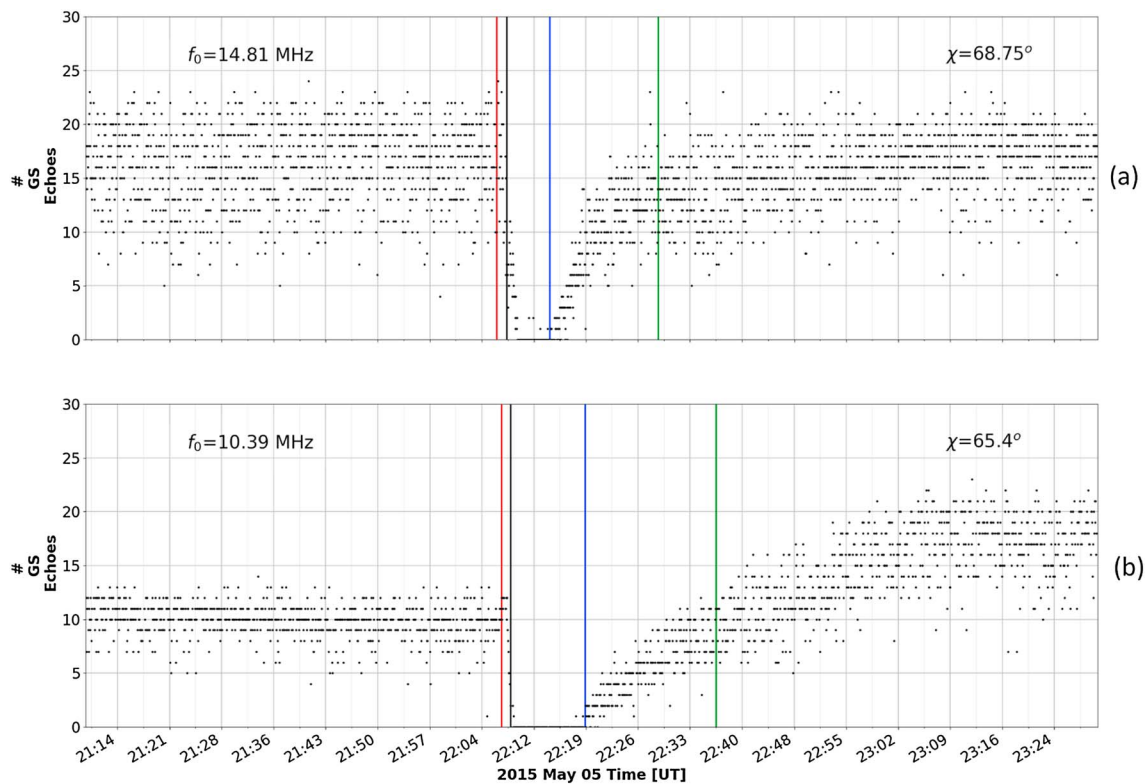


**Figure 6.** Comparison of ground scatter echoes during a SWF event on 5 May 2015 observed by the (a) BKS and (b) KAP radars. Similar format to Figure 4c. These measurements correspond to similar solar zenith angle ( $\chi$ ) but different radar operating frequencies ( $f_0$ ).

SWF is a dayside phenomenon and most impactful at the subsolar point. So here we are going to examine the solar zenith angle effect on SWF signature. Figure 5 shows the impact of solar zenith angle (SZA,  $\chi$ ) on the intensity and duration of SWF. Note that the radars shown in Figure 5 were operating at different frequencies. When ground scatter is generated, radio signal crosses the  $D$  region a total of 4 times at two different locations (assuming the inbound and outbound ray path is symmetrical), one nearer to the radar site and the other farther from the radar site. We elect to characterize the features of SWF in terms of a single value of SZA for a set of radar observation at a given time. We take the average of the SZA values of  $D$  region penetration points for the central beam as the representative value of SZA. Note that the variability of SZA across the radar field of view is much smaller ( $\leq 10\% \approx 2^\circ - 3^\circ$ ) than the variation in SZA across the radar sites, justifying the use of an average value of SZA to characterize the individual radar observations. Vertical lines passing through each panel show the phase timings of SWF observed by the individual radars. Red, black, blue, and green lines indicate onset, blackout, start of recovery, and end of recovery, respectively. Radars located closest to the subsolar point (e.g., PGR and CVW) are impacted more severely than the radars located farther away from the subsolar point (e.g., GBR and BKS), indicating that SZA controls the intensity of SWF signatures. Effects can be seen in the duration of the event, as well as in the durations of blackout and recovery phases and the depth of the blackout phase (% change in the number of ground scatter during the blackout phase). Also, note that the recovery of the radars having smaller SZA (e.g., PGR and CVW) is more gradual than that of radars with higher SZA (e.g., BKS and GBR).

Just like SZA, frequency of the propagating radio wave also alters the signatures of SWF. The nondeviative absorption of a radio wave in the ionosphere has an inverse second-power dependency on the frequency of the radio wave, so the lower the frequency of the radio wave, the more it is attenuated. Figure 6 compares the response of SWF between two radars with similar SZA but different operating frequencies. A stronger SWF response was observed by the radar operating at a lower frequency (KAP), and the recovery phase was more gradual. Taken together, both figures show neither SZA nor operating frequency plays a major role in influencing the timing and duration of onset phase.

**Table 1**  
*Events List for Statistical Study*

Event (UTC)	Duration (minutes)	Flare class
2015/5/5 22:10:00	90	X2.7
2015/3/11 16:22:00	90	X2.2
2014/9/10 17:45:00	60	X1.7
2013/5/13 16:05:00	75	X2.9
2014/3/29 17:48:00	50	X1.0
2014/2/25 00:49:00	70	X5.0
2014/4/25 00:27:00	70	X1.4
2013/5/15 01:48:00	80	X1.3
2013/11/5 22:12:00	130	X3.4

Note. Event dates are formatted as year/month/day.

<sup>a</sup>Events are associated with X class flares. <sup>b</sup>On an average, five radars are affected by each of these events that gives a total = 52 radar events.

### 3.2. Statistical Results

In order to characterize statistical behavior of SWF signatures in SuperDARN data, we choose nine different X class events from 2013 to 2015. We consider GOES X-ray sensor instruments as our reference to identify these events. Table 1 provides a list of event times, event duration, and solar flare class associated with all the events used in this statistical study. Each event generally lasts for  $\approx 50$  min to an hour and a half and affects five radars on average, so a total of 52 SWF signatures were analyzed from SuperDARN radars across the Northern Hemisphere. Figure 7 shows an analysis correlating the durations of SWF phases with SZA, radio wave frequency, and solar flare intensity. It can be seen that the short-lived onset phase (upper row) has a relatively weak dependence on all three parameters, while the long-lived blackout and recovery phase duration shows higher dependence on all three parameters, especially with SZA and frequency. Also, SZA has a negative correlation with all phase durations; that is, the SWF impact was mitigated with increasing SZA. Again, frequency (middle column) and solar flare intensity (right column) show relatively less influence on the phase durations.

In order to describe different phases of SWF as a linear function of SZA, frequency, and peak solar flux, we do a multiple linear regression analysis. Figure 8 shows multiple linear regression models of the phase durations as a function of the physical parameters discussed above. The models do a reasonably good job reproducing the durations of blackout and recovery phase (i.e., the correlation coefficient is high) but not so well for the onset phase. Note that based on the analysis in Figure 7, it is expected that none of the parameters  $\chi$ ,  $f_0$ , and  $\Phi_0$  can adequately reproduce onset phase.

In order to find the typical durations of the SWF phases and characterize average radar observations, we do a superposed epoch analysis on 52 radar signatures. Figure 9 shows a superposed epoch analysis of all SWF events, taking maximum absorption time (radio blackout start time) as the key time (0.0 hr). The first three panels are color coded by SZA, frequency, and solar flare intensity, while the last panel shows the average duration of the three SWF phases. The black thick line passing through all panels is the mean value of all events, while the standard deviation error bars given in red and thin color lines are for the individual events. In panels (a)–(c) all event signatures lying below the black line (average signature) have a more severe impact. Brighter colors correspond to higher values of SZA, frequency, and flare intensity. Based on the correlation coefficients obtained by the statistical study, we can conclude that SZA is the dominant parameter, which is consistent with Figure 7. Panel (d) shows the mean duration of different phases for any typical SWF event (average values), are 100 s, 10 min 33 s, and 41 min 45 s for onset, radio blackout, and recovery phases, respectively.

Next, we examine the statistical behaviors of the Doppler flash feature of SWF. Figure 10 shows a statistical analysis of the Doppler flash phenomenon. Figures 10a–10c are scatter plots of peak Doppler velocity versus SZA, radio wave frequency, and solar flare intensity. It can be seen that the peak value of the Doppler velocity has a relatively weak dependence on SZA (panel a) and solar flare intensity (panel c), but stronger dependence on frequency (panel b). Also, SZA and frequency have a negative correlation; that is, with increasing SZA, peak Doppler velocity value decreases, while it increases with peak flare intensity.



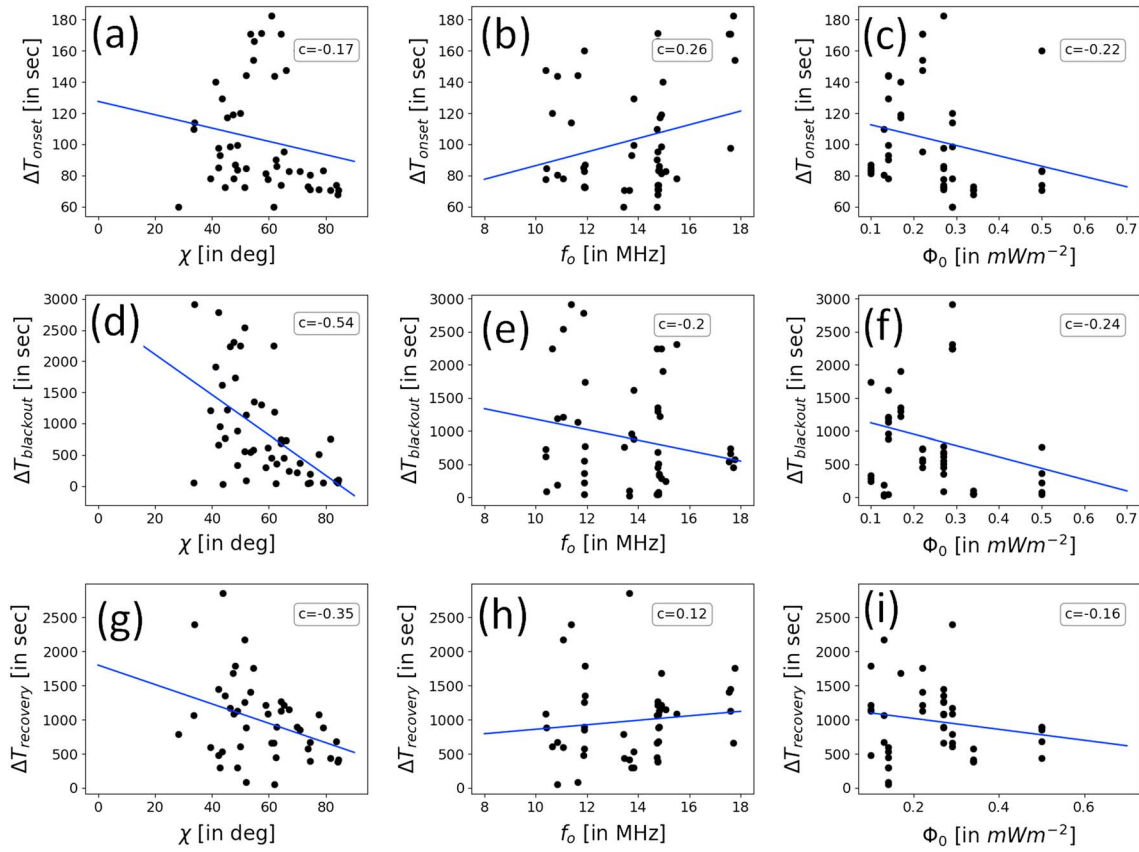


**Figure 7.** Scatter plots of duration of onset phase  $\Delta T_{onset}$  (a–c), duration of blackout phase  $\Delta T_{blackout}$  (d–f), and duration of recovery phase  $\Delta T_{recovery}$  (g–i) versus SZA ( $\chi$ , left column), operating frequency ( $f_o$ , center column), and solar X-ray flux ( $\Phi_0$ , right column). Blue lines show the best fitted value, and the associated correlation coefficients are also provided inside each panel.

Figures 10a–10c show variation of the peak Doppler velocity with respect to SZA, frequency, and peak solar flux ( $\chi$ ,  $f_o$ , and  $\Phi_0$ ), respectively. Note that the variation in the data set along the y axis is mostly due to other parameters ( $f_o$ ,  $\Phi_0$ ), ( $\chi$ ,  $\Phi_0$ ) and ( $\chi$ ,  $f_o$ ). To obtain individual functional forms of peak Doppler velocity with respect to all physical parameters under consideration (SZA or frequency or peak solar flux), we averaged out the effects of the other parameters by taking the mean from the Doppler velocity data and fitting a curve through it. To obtain the functional form of Doppler velocity with respect to SZA, we binned the data into

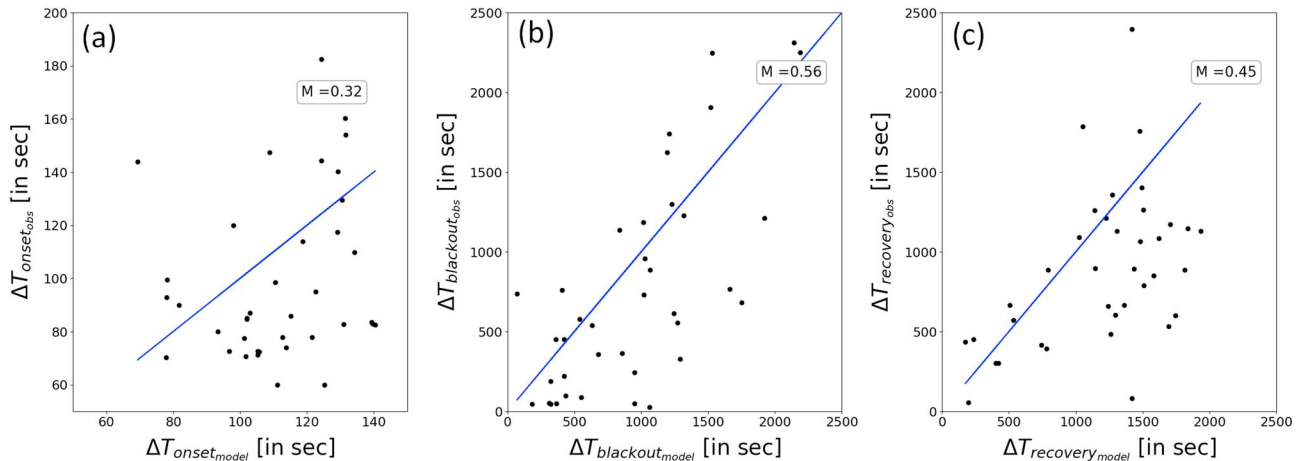


**Figure 8.** Multiple regression scatter plots of predicted (a)  $\Delta T_{onset}$ , (b)  $\Delta T_{blackout}$ , and (c)  $\Delta T_{recovery}$  versus corresponding measured values from a multiple linear regression model. Blue lines show the best fitted values, and the correlation coefficients are provided inside each panel.

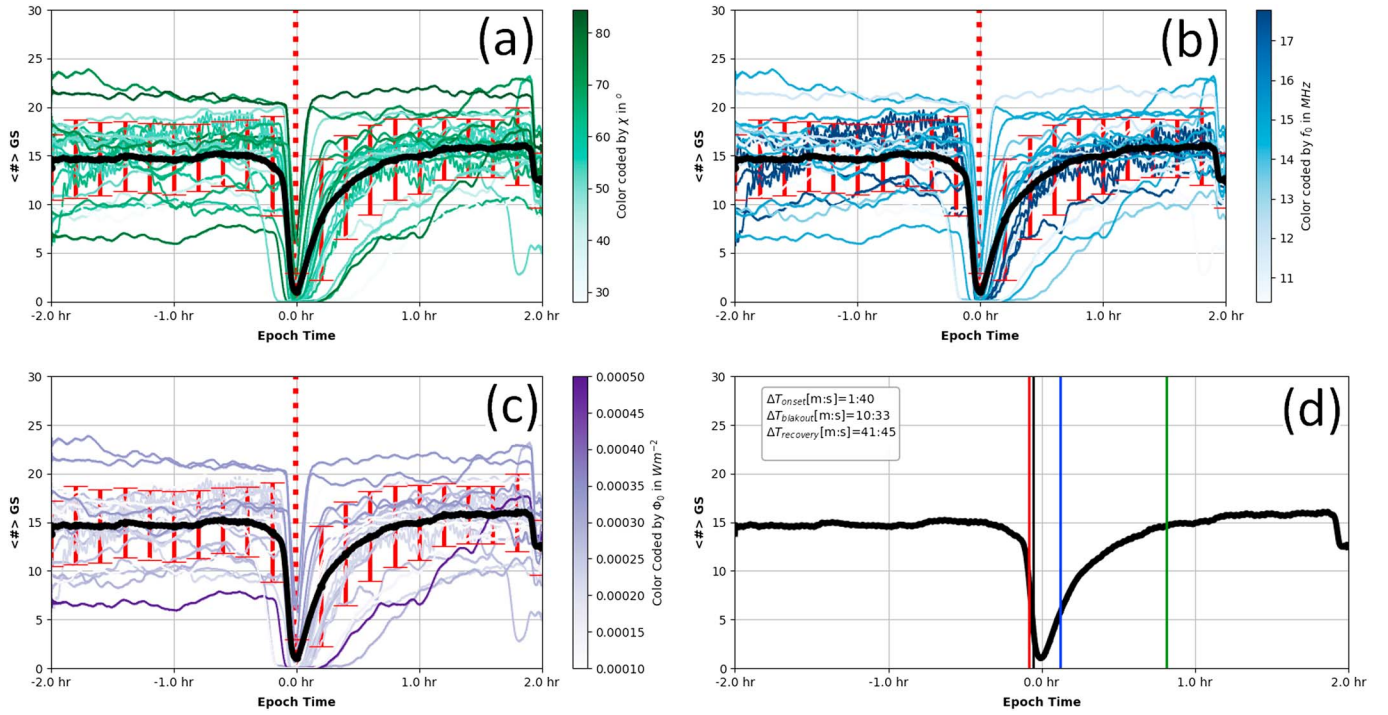


**Figure 9.** Superposed epoch analysis of ( $\approx 52$ ) SWF signatures seen by SuperDARN radars during the nine X class solar flares listed in Table-1. Panels (a)–(c) respectively show the ground scatter echoes color coded by SZA ( $\chi$ ), frequency ( $f_0$ ), and solar X-ray flux  $\Phi_0$ . Panel (d) shows average timings of onset (red), blackout start (black), blackout end (blue), and recovery (green). Duration of each phase is also provided inside the panel.

groups with respect to SZA and used the average values of the data to represent the Doppler velocity for that bin. We repeat this similar procedure for frequency and peak X-ray flux as well. Scatter plots in Figures 10d–10f show the variation in Doppler velocity with respect to only one of the physical parameters ( $\chi$ ,  $f_0$ , and  $\Phi_0$ , respectively). Now we want to fit a curve through the data shown in Figures 10d–10f to obtain best fitted individual functional forms of Doppler velocity, but we do not know the exact functional form of Doppler velocity with respect to all the parameters under consideration. However, Doppler velocity provides the proxy measure of decrease in phase path length which is the effect of decrease in refractive index or increase in plasma density (plasma frequency; Kikuchi et al., 1986; Watanabe & Nishitani, 2013). Assuming that the ionospheric density conforms to a Chapman function and making use of binomial approximation (on the nondeviative absorbing  $D$  layer; Davies, 1990) the refractive index can be expressed as

$$\eta \approx 1 - \frac{k}{2} \frac{g(\Phi_0)}{f_0^2} e^{1-z-\sec \chi} e^{-z} \quad (1)$$

where,  $k$  is constant,  $z$  is the scale height, and  $(\Phi_0)$  is the functional dependence of incoming solar flux and ionization, which is typically linear for fixed wavelength. In order to obtain the functional form of  $\eta$  in terms of  $\chi$ ,  $f_0$ , and  $\Phi_0$  only, we simply integrate (analytical integration) equation (1) with respect to  $(f_0, \Phi_0)$ ,  $(\chi, \Phi_0)$ , and  $(\chi, f_0)$ , respectively. The functional dependence of  $\eta$  with SZA, frequency, and solar flux are  $e^{a-b \sec \chi}$ ,  $a - \frac{b}{f_0^2}$ , and  $a + b \log_{10} \Phi_0$ , respectively. Applying this approach yields Figures 10d–10f, where black lines show the fitted functional forms which are reasonably close to the measured velocities.

In order to examine the timing of the Doppler flash relative to the SWF we did a superposed epoch analysis of multiple events. Figure 10g shows superposed epoch analysis of all Doppler flash events, taking maximum absorption time (radio blackout start time) as the key time (0.0 hr). The blue thick line is the median value of all events, while the standard deviation error bars are provided in red. Panel (d) shows that the Doppler flash consistently occurs before the radio blackout phase (red dashed line) and reaches a typical value of 90–100 m/s.

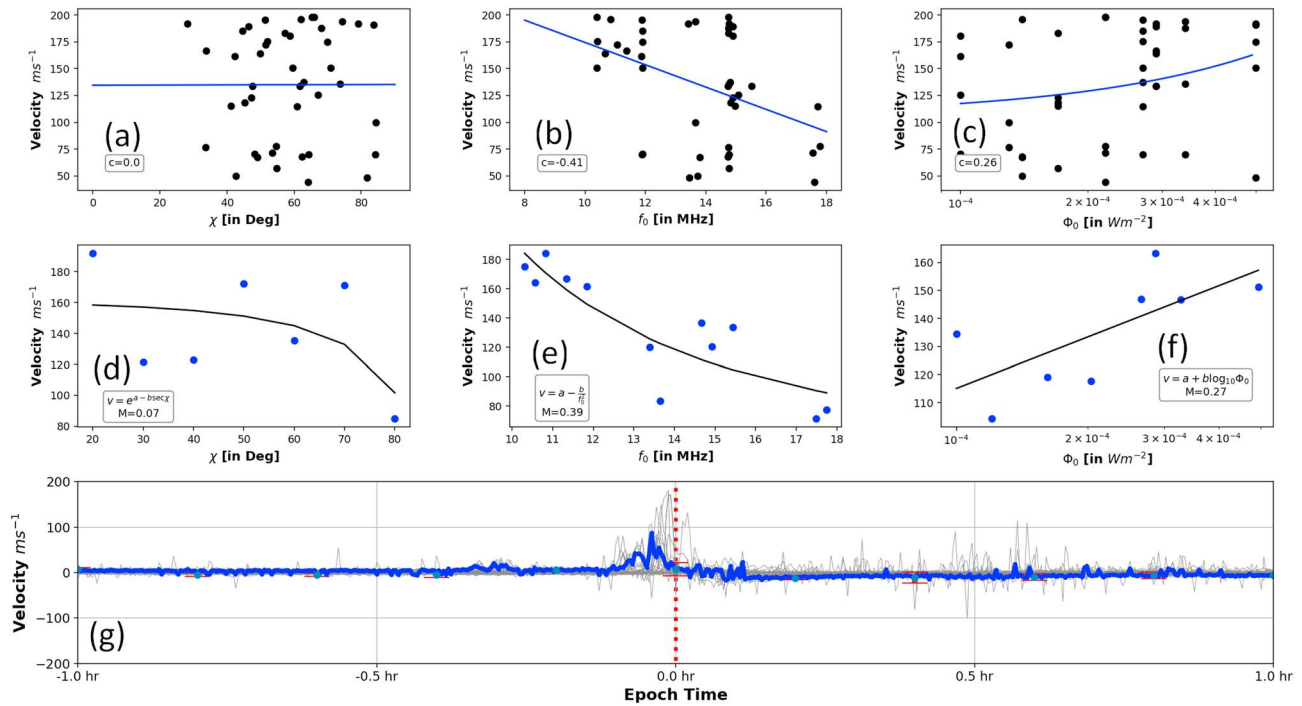


**Figure 10.** Statistical analysis of peak Doppler flash data from multiple events. Panels (a)–(c) respectively show scatter plots of peak Doppler flash versus SZA ( $\chi$ ), frequency ( $f_0$ ) and solar X-ray flux  $\Phi_0$ . Blue lines show the best fitted values and the correlation coefficients are provided inside each panel. Panels (d)–(f) show the functional dependence of peak velocity with only SZA ( $\chi$ ), only frequency ( $f_0$ ) and only solar X-ray flux  $\Phi_0$  respectively (see text for details). Black lines show the best fit curves, while the box inside the panels shows the functional forms and the multiple linear regression correlation coefficients. Panel (g) shows a superposed epoch analysis of SuperDARN Doppler velocity using radio blackout as the key time (vertical dashed red line, 0.0 hr).

#### 4. Discussion

This paper provides a characterization of SWF detected by SuperDARN radars in response to nine X class flares occurring in 2013–2015. This section summarizes the main findings and compares with the results of the previous studies.

SWF is the most significant effect seen by HF communication systems following a solar flare event and drop in HF signal strength is the most well-known feature of SWF as described by many previous studies (Davies, 1990; Mitra, 1974). Figures 2 to 6 show evidence of decreased backscatter signal in SuperDARN observations most likely due to increased *D* region nondeviative absorption (Benson, 1964; McNamara, 1978; Zawdie et al., 2017). The signature of SWF in SuperDARN daytime observation has three distinct phases, namely, onset, blackout, and recovery with typical durations of 100 s, 10 min, and 42 min, respectively. We have examined the dependencies of the SWF phases on SZA, radar frequency, and peak solar X-ray flux and found that the long-lived phases (blackout and recovery) have significant dependencies on all three physical parameters. The study by Xiong et al. (2013) showed that the ionospheric solar flare activity indicator (ISFAI, TEC data) that describes average ionospheric effects in response to solar flares has a high statistical correlation with SZA, which is consistent with our results for the long-lived blackout and recovery phases. Radar frequency also alters the signature of the SWF event as shown in Figure 6. Radars operating at low frequency experience a deeper and longer-lived SWF effect. A recent study done by Eccles et al. (2005) reported an inverse-square frequency dependence of the radio wave absorption during SWF. The study estimated the frequency dependence of absorption using the physics-based ABBY Normal model and validated the result against an empirical data-driven model obtained from the HDIVE experiment. The ABBY Normal model only estimates the absorption of radio signal for the case of normal ionospheric incidence. The SuperDARN results could be used to modify the functionality of the model and to estimate the ionospheric losses during multihop propagation.

Statistical analysis reveals that among the three different phases the short-lived onset phase has a weak dependence on the parameters under consideration (SZA, radar frequency, and peak flux density). The onset phase is very brief and simultaneous across all the radars on the dayside of the Earth, irrespective of SZA or radar frequency. The variation in the arrival time of enhanced electromagnetic (EM) radiation from the Sun

is negligible across the dayside of the Earth, which leads to a very brief and simultaneous onset. The transition to the blackout phase is very rapid ( $\leq 100$  s). This dramatic timing suppresses the effects of all controlling parameters such that they have no influence on the duration of the onset phase. The identification of the onset phase in the SuperDARN radar observations is a significant advancement in the understanding of SWF and was lacking in the prior studies.

Statistical results show that the long-lived phases (blackout and recovery) of the SWF have significant dependencies on all three parameters under considerations (SZA, radar frequency, and peak flux density). A deeper and longer impact can be seen for the radars having a lower SZA, as ionospheric absorption effects are modified by the cosine factor with respect to SZA. Also, radars operating at lower frequencies observe a more severe impact due to the inverse-square dependence on frequency. However, peak X-ray flux seems to have significantly less impacts on the SWF signature. The correlation coefficients shown in Figure 7 for blackout and recovery phases with peak X-ray flux intensity are lower than those for SZA and radar frequency. The reason for the small correlation between peak X-ray flux and the phases of SWF is likely due to the fact that peak X-ray flux does not provide a good representation of the total ionization energy deposited in the upper atmosphere due to flare-enhanced EUV and X-ray fluxes. During flare events the integrated flux from these bands contributes to the ionization energy deposition in the lower regions of upper atmosphere. A recent study by Le et al. (2011) showed that the peak X-ray intensity is not a good proxy of EUV flux and that an adjustment of the cosine factor with respect to central meridional distance (CMD - location of the flare on the solar disk) leads to a better correlation between these bands. Future work will characterize the spatiotemporal dependence of the SWF signature on the ionization due to flare-enhanced EUV and X-ray radiation.

One of the fascinating features of the SWF signature is the Doppler flash that precedes the suppression of ground scatter. Most HF communication systems observe a drop in signal strength during an SWF event, but SuperDARN provides more insights into the initial phase and nature of SWF phenomenon by measuring phase information in the form of an apparent Doppler velocity. Figure 4d shows a clear example, while Figure 10 presents statistics and functional dependencies with the selected physical parameters. We found that the peak value of Doppler velocity has a comparatively weak dependence on SZA and peak X-ray flare but a relatively stronger dependence on radar frequency. Superposed epoch analysis in Figure 10g shows that the Doppler flash feature precedes the radio blackout and the equivalent Doppler velocity reaches a typical value of  $\approx 100$  m/s. A sudden increase in apparent Doppler velocity occurs due to phase shift, which implies a reduction in phase path length of the propagating radio wave. Kikuchi et al. (1986) described this phenomenon as being possibly due to two separate factors, one being the apparent decrease in the phase path length as a result of the change in the refractive index caused by increasing electron densities in the *D* region (nondeviating slab) ionosphere and the other being the phase length decrease because of the descent of the reflection point associated with increasing electron density in the *F* region ionosphere. A more recent study by Watanabe and Nishitani (2013) using SuperDARN Hokkaido radar data found that the decrease in phase path length mechanism was more consistent with observations in a case study. Also, previous study by Handzo et al. (2014) showed that Digisonde observed an enhancement in plasma frequency in the lower regions of the ionosphere during a flare event. Both of these studies suggest that SWF is a lower ionospheric space weather phenomenon. The Doppler flash feature can also be analyzed as arising from a change in conductivity of the ionosphere, which leads to a change in phase path of the EM wave. Another study done by Siskind et al. (2017) showed that ionospheric absorption peaks at the lower *E* region and *D* region of the ionosphere where the ionization maximizes due to enhancement of X-ray and EUV flux. Clearly, the Doppler flash and *D* and *E* region absorption phenomenon are related and have similar driving processes. Further detailed analysis and modeling of the Doppler flash phenomenon may provide further insights into the initial ionospheric response to solar flares and to the underlying physics of SWF phenomena.

## 5. Conclusion and Future Work

The main purpose of this paper has been to statistically characterize the signature of SWF in SuperDARN ground scatter observations and to describe the dependence of phase timings, duration of the phases and depth of blackout and dependencies on physical parameters such as solar zenith angle, operating frequency, and intensity of the solar flare. Another objective was to identify and characterize the Doppler flash feature and provide functional dependence of peak Doppler velocity with zenith angle, frequency, and solar flux. Results show that the effects in the HF radar observations are mostly controlled by solar zenith angle and less by radar frequency and flare intensity, whereas peak Doppler velocity is mostly dependent on radar



operating frequency. None of the physical parameters investigated in this study are able to influence strongly the onset phase timing and duration across different radars, while blackout and recovery depend on initial conditions. Future work will examine how SWF characteristics may depend on season, solar cycle,  $F_{10.7}$ , and geomagnetic activity indices, also, how EM wave propagation through  $D$  region alters under SWF conditions.

## Acknowledgments

We thank the National Science Foundation for support under grant AGS-1341918. We wish to acknowledge the use of the NOAA/GOES X-ray data (from <https://satdat.ngdc.noaa.gov/sem/goes/data/>) for flare confirmation and analysis. We also thank all participants in the worldwide SuperDARN collaboration for the distribution of SuperDARN data via <http://vt.superdarn.org/tiki-index.php?page=Data+Access>. The majority of analysis and visualization was completed with the help of free, open-source software tools such as matplotlib (Hunter, 2007), IPython (Pérez & Granger, 2007), pandas (McKinney, 2010), Skifield python API, and others (e.g., Millman & Aivazis, 2011).

## References

- Afraimovich, E. L. (2000). GPS global detection of the ionospheric response to solar flares. *Radio Science*, 35(6), 1417–1424.
- Benson, R. F. (1964). Electron collision frequency in the ionospheric D region. *Radio Science*, 68D(10). Retrieved from [https://nvlpubs.nist.gov/nistpubs/jres/68D/jresv68Dn10p1123\\_A1b.pdf](https://nvlpubs.nist.gov/nistpubs/jres/68D/jresv68Dn10p1123_A1b.pdf)
- Chisham, G., Lester, M., Milan, S., Freeman, M., Bristow, W., Grocott, A., et al. (2007). A decade of the Super Dual Auroral Radar Network (SuperDARN): Scientific achievements, new techniques and future directions. *Surveys in Geophysics*, 28, 33–109. <https://doi.org/10.1007/s10712-007-9017-8>
- Davies, K. (1990). *Ionospheric radio*. London, UK: Peter Peregrinus Ltd.
- Dellinger, J. (1937). Sudden disturbances of the ionosphere. *Proceedings of the Institute of Radio Engineers*, 25, 1253–1290.
- DeMastus, H., & Wood, M. (1960). Short-wave fadeouts without reported flares. *Journal of Geophysical Research*, 65(2), 609–611.
- Eccles, J. V., Hunsucker, R. D., Rice, D., & Sojka, J. J. (2005). Space weather effects on midlatitude HF propagation paths: Observations and a data-driven D region model. *Space Weather*, 3, S01002. <https://doi.org/10.1029/2004SW000094>
- Ellison, M. A. (1996). The solar flare radiation responsible for sudden frequency deviation and geomagnetic fluctuation. *Journal of Geophysical Research*, 101, 10,855–10,862.
- Greenwald, R. A., Baker, K. B., Hutchins, R. A., & Hanuise, C. (1985). An HF phased-array radar for studying small-scale Structure in the high-latitude ionosphere. *Radio Science*, 20(1), 63–79. <https://doi.org/10.1029/RS020i001p00063>
- Handzo, R., Forbes, J. M., & Reinisch, B. (2014). Ionospheric electron density response to solar flares as viewed by digisondes. *Space Weather*, 12, 205–216. <https://doi.org/10.1002/2013SW001020>
- Hunter, J. D. (2007). Matplotlib: A 2D graphics environment. *Computing In Science & Engineering*, 9(3), 90–95. <https://doi.org/10.1109/MCSE.2007.55>
- Kikuchi, T., Sugiuchi, T., Ishimine, M. H., & Shigehisa, H. (1986). Solar-terrestrial disturbances of June–September 1982. IV. Ionospheric disturbances. 11. HF Doppler observations. *Journal of the Radio Research Laboratory*, 33(1), 239–255.
- Le, H., Lui, L., He, H., & Wan, W. (2011). Statistical analysis of solar EUV and X-ray flux enhancements induced by solar flares and its implication to upper atmosphere. *Journal of Geophysical Research*, 116, A11301. <https://doi.org/10.1029/2011JA016704>
- McKinney, W. (2010). Data structures for statistical computing in python. In S. van der Walt & J. Millman (Eds.), *Proceedings of the 9th Python in Science Conference* (pp. 51–56). Austin, TX: Python in Science Conference.
- McNamara, L. F. (1978). Statistical model of D region. *Radio Science*, 14(6), 1165–1173.
- Mendillo, M., & John, E. (1974). Incoherent scatter observations of the ionospheric response to a large solar flare. *Radio Science*, 9(2), 197–203.
- Millman, K. J., & Aivazis, M. (2011). Python for scientists and engineers. *Computing in Science & Engineering*, 13(2), 9–12. <https://doi.org/10.1109/MCSE.2011.36>
- Mitra, A. (1974). *Ionospheric effects of solar flare, vol. 46, Astrophysics and space science library*. Massachusetts: Reading. <https://doi.org/10.1007/978-94-010-2231-6>
- Mitra, A. P., & Shain, C. A. (1953). The measurement of ionospheric absorption using observations of 18.3 Ms/s cosmic radio noise. In *Journal of Atmospheric and Terrestrial Physics* (Vol. 4). London: Pergamon Press Ltd.
- Newton, H. W., & Barton, H. J. (1937). Bright solar eruptions and radio fadings during the years 1935–36. *Monthly Notices of the Royal Astronomical Society*, 97, 594–611.
- Pérez, F., & Granger, B. E. (2007). IPython: A system for interactive scientific computing. *Computing in Science and Engineering*, 9(3), 21–29. <https://doi.org/10.1109/MCSE.2007.53>
- Siskind, D. E., Zawdie, K., Sassi, F., Drob, D., & Friedrich, M. (2017). Global modeling of the low- and middle-latitude ionospheric D and lower. *E Regions and Implications for HF Radio Wave Absorption, Space Weather*, 15, 115–130. <https://doi.org/10.1002/2016SW001546>
- Tsurutani, B. T., Guarnieri, F. L., Fuller-Rowell, T., Mannucci, A. J., Iijima, B., Gonzalez, W. D., et al. (2006). Extreme solar EUV flares and ICMEs and resultant extreme ionospheric effects: Comparison of the Halloween 2003 and the Bastille day events. *Radio Science*, 41, RS5507. <https://doi.org/10.1029/2005RS003331>
- Watanabe, D., & Nishitani, N. (2013). Study of ionospheric disturbances during solar flare events using the SuperDARN Hokkaido radar. *Advances in Polar Science*, 24(1), 12–18. <https://doi.org/10.3724/SPJ.2013.00012>
- Xiong, B., Wan, W., Ning, B., Ding, F., Hu, L., & Yu, Y. (2013). A statistic study of ionospheric solar flare indicator. *Space Weather*, 12, 29–40. <https://doi.org/10.1002/2013SW001000>
- Zawdie, K. A., Drob, D., Siskind, D. E., & Coker, C. (2017). Calculating the absorption of HF radio waves in the ionosphere. *Radio Science*, 52, 767–783. <https://doi.org/10.1002/2017RS006256>